Local normal vector field formulation for periodic scattering problems formulated in the spectral domain

Document Version:
Accepted manuscript including changes made at the peer-review stage

Please check the document version of this publication:

• A submitted manuscript is the version of the article upon submission and before peer-review. There can be important differences between the submitted version and the official published version of record. People interested in the research are advised to contact the author for the final version of the publication, or visit the DOI to the publisher's website.
• The final author version and the galley proof are versions of the publication after peer review.
• The final published version features the final layout of the paper including the volume, issue and page numbers.

Link to publication

Local normal-vector-field formulation for periodic scattering problems formulated in the spectral domain

M.C. VAN BEURDEN[1,*] AND I.D. SETIJA[2]

[1]*Faculty of Electrical Engineering, Eindhoven University of Technology, P.O. Box 513, 5600 MB Eindhoven, The Netherlands*
[2]*ASML Netherlands B.V., De Run 6501, 5504 DR, Veldhoven, The Netherlands*
[*]*Corresponding author: M.C.v.Beurden@tue.nl*

We present two adapted formulations, one tailored to isotropic media and one for general anisotropic media, of the normal-vector field framework previously introduced to improve convergence near arbitrarily shaped material interfaces in spectral simulation methods for periodic scattering geometries. The adapted formulations enable the definition and generation of the normal-vector fields to be confined to a region of prolongation that includes the material interfaces but is otherwise limited. This allow for a more flexible application of geometrical transformations like rotation and translation per scattering object in the unit cell. Moreover, these geometrical transformations enable a cut-and-connect strategy to compose general geometries from elementary building blocks. The entire framework gives rise to continuously parameterized geometries. © 2016 Optical Society of America

OCIS codes: *(050.1755) Computational electromagnetic methods; (050.1950) Diffraction gratings.*

1. INTRODUCTION

The concept of normal-vector fields, as introduced in [1], has been adopted in several computational frameworks to improve the convergence in a Fourier basis, in particular in the differential method [1, 2], the rigorous coupled wave analysis (RCWA) [3], and more recently in the volume-integral method [4–6]. The basic idea behind this concept is that normal-vector fields can separate the components of the electric field (*E*) and the electric flux density *D*. Via this separation, we can access the continuous components of both *E* and *D* across material interfaces and construct a vector field *F* that is continuous everywhere, with the possible exception of isolated points and lines that correspond to geometrical edges and corners of the scattering object under investigation. By introducing the concept of a normal-vector field, field-material interactions in a spectral basis via the vector field *F* demonstrate improved accuracy, compared to field-material interactions acting on either *E* or *D*. This leads to improved characterization of reflection coefficients at lower computational costs.

However, one of the challenges of the normal-vector-field concept is the actual generation of the normal-vector field itself on the domain of computation. There are very few constraints to generate such a vector field, but at the same time there are open questions related to its generation. A desirable property is for instance to construct a continuously varying normal-vector field for a continuously varying geometry of

the scattering object in the unit cell. If the normal-vector field exhibits discontinuous behavior as a function of a geometrical parameter that is being varied, the discontinuous behavior can lead to non-smooth behavior in certain field quantities, which in turn can give rise to discontinuous parameter derivatives. In a gradient-based optimization algorithm, for instance in a design or inverse-scattering approach, discontinuous parameter derivatives are known to significantly affect the convergence of the optimization algorithm. A further requirement for the generation of normal-vector fields is the time needed to set up a normal-vector field. This computational overhead should be as low as possible, to allow for fast analysis and reconstruction algorithms. One quite general approach to generate normal-vector fields has been put forward in [7, 8], based on scattered-data interpolation.

A disadvantage of the existing normal-vector-field formulation is that the normal-vector field is required on the *entire* computational domain [1, 3, 7]. As a consequence, one cannot operate on isolated domains without taking care of connecting interfaces. Here, we will demonstrate that it is possible to arrive at a formulation that requires the normal-vector field only locally, both for isotropic and anisotropic dielectric media. More importantly, this enables a cut-and-connect technique with basic building blocks that allow for a rapid and flexible generation of a normal-vector field and the corresponding Fourier integrals for the field-material interactions for more complicated shapes. This also addresses the above mentioned issues regarding setup

time and continuity under geometry changes, by employing parameterized building blocks with normal-vector fields that vary continuously as a function of the shape parameters.

2. FIELD-MATERIAL INTERACTIONS IN THE SPECTRAL DOMAIN

For any of the spectral expansion methods, like RCWA, the Differential method, or the spectral volume integral method, the electric field E and the electric flux density D are expanded in terms of a Fourier basis in the transverse plane (x, y) as

$$E = \sum_{m \in \mathbb{Z}^2} e_m(z) \exp\{-j[(k_x^i + k_x^m)x + (k_y^i + k_y^m)y)]\}, \quad \textbf{(1a)}$$

$$D = \sum_{m \in \mathbb{Z}^2} d_m(z) \exp\{-j[(k_x^i + k_x^m)x + (k_y^i + k_y^m)y)]\}. \quad \textbf{(1b)}$$

where k_x^i and k_y^i form the linearly progressing phase of the incident field and (k_x^m, k_y^m) form the Bravais lattice that is reciprocal to the spatial lattice of the periodic setup in the xy-plane.

The normal-vector field formulation in [1] can be seen as a member of the family of Fourier factorization rules, which were first empirically discovered in [9, 10] and subsequently systematically developed and formulated by Li [11]. The Fourier factorization rules provide a framework for computing the coefficients d_m from e_m, and vice versa, when the permittivity function exhibits discontinuities in the transverse plane. Material discontinuities in the transverse plane cause problems in the convergence of the Fourier series expansions for the electric flux density and electric field when the permittivity function is straightforwardly written as a standard truncated discrete convolution, i.e. the Laurent rule. The key idea to overcome these convergence issues is to apply the permittivity function and inverse permittivity function to the continuous components of the electric field and the electric flux density and derive expressions for the discontinuous components of D and E. The resulting constitutive relation between D and E in the spectral domain is then a balanced combination of the Laurent rule, i.e. the discrete convolution in the form of a Toeplitz matrix for the permittivity $\varepsilon(x, y, z)$, and the inverse rule, i.e. to apply the inverse matrix of the Toeplitz matrix for $1/\varepsilon(x, y, z)$. The framework formulated in [11] is most straightforward in cases when both the periodicity and the discontinuities in the permittivity are $x - y$ oriented, whereas the normal-vector field formulation put forward by Popov and Nevière [1] is more amenable for material discontinuities of curved and more complicated geometries.

A. Summary of results by Popov and Nevière

The vector field F_ϵ is introduced in [1] (below Eq. (8)) as a mix between the electric field E and the electric flux density D, such that the vector field F_ϵ is continuous across an interface between two media. To this end, a normal-vector field $N(r)$ and two tangential-vector fields, i.e. $T_1(r)$ and $T_2(r)$, are defined on the entire unit cell of the configuration. The normal-vector field is normal to every material interface and both tangential-vector fields are tangential to every material interface, with the possible exceptions at sharp edges and corners. The vector field F_ϵ is then defined as

$$F_\epsilon = \begin{pmatrix} T_1 \bullet E \\ N \bullet D \\ T_2 \bullet E \end{pmatrix}, \quad \textbf{(2)}$$

where $\bullet$ indicates the usual local real-valued vectorial inner product. Subsequently, the two field-material operators C_ϵ and $\overline{\overline{\epsilon}} \bullet C_\epsilon$ are derived such that (see Reference [1] below Eq. (12)),

$$E = C_\epsilon F_\epsilon, \quad \textbf{(3a)}$$

$$D = \overline{\overline{\epsilon}} \bullet C_\epsilon F_\epsilon. \quad \textbf{(3b)}$$

Since the vector field F_ϵ is continuous throughout, the Fourier factorization rules allow the operations defined in Eq. (3) to be written as a matrix-vector product in the spectral domain, i.e. the elements C_ϵ and $\overline{\overline{\epsilon}} \bullet C_\epsilon$ can be computed in the spectral domain and the matrix-vector product with F_ϵ can be executed according to the Laurent rule, i.e. via standard discrete convolutions. This discrete convolution structure can be further exploited numerically via Toeplitz matrices or Fast Fourier Transforms.

B. Revised normal-vector-field formulation

The above formulation in terms of normal-vector and tangential-vector fields has the disadvantage that these vector fields are required on the entire computational domain and that each scattering setup requires a newly generated set of these fields. To make the normal-vector field approach more generic and modular, we first reformulate the above in terms of projection operators.

We introduce the operator P_n as

$$P_n v = N(N \bullet v), \quad \textbf{(4)}$$

where v is an arbitrary 3D vector field. From the properties of the normal-vector field N, we observe that P_n is a projection operator and therefore it is idempotent, i.e. $P_n P_n = P_n$. Similarly, we can introduce the operator P_T as

$$P_T v = T_1(T_1 \bullet v) + T_2(T_2 \bullet v), \quad \textbf{(5)}$$

which is also a projection operator. Besides the idempotency property, the projection operators P_T and P_n have two other useful properties. We have $P_T = I - P_n$, where I is the identity operator. This property shows that the normal-vector field itself is sufficient to generate both the operator P_n and the operator P_T, which was already observed from the construction of the tangential-vector fields. Also, the operator P_T is mutually orthogonal to P_n, i.e. $P_T P_n = P_n P_T = 0$.

With these projection operators, a vector field F is constructed as

$$F = P_T E + \alpha P_n D = (I - P_n)E + \alpha P_n D. \quad \textbf{(6)}$$

where α is a non-zero scaling function, which is continuous across material interfaces. This is a slightly, but vitally, different definition of the vector field F_ϵ and to indicate the difference, we have dropped the subscript ϵ. The first difference regards the scaling function α, which has two main consequences. This can bring the scale of the components of the vector field F to the same order of magnitude. This can improve the conditioning of the matrix representations C_ϵ and $\overline{\overline{\epsilon}} \bullet C_\epsilon$. Also, and more importantly, it has far-reaching consequences for the size of the domain on which the normal-vector field N is required, as will be demonstrated shortly. The second difference between F and F_ϵ is that the components of F are expressed in terms of a global basis that is independent of N, e.g. in the Cartesian coordinate

system as

$$\boldsymbol{F} = \begin{pmatrix} F_x \\ F_y \\ F_z \end{pmatrix} = \begin{pmatrix} F_n(\boldsymbol{N} \bullet \boldsymbol{u}_x) + F_{T_1}(\boldsymbol{T}_1 \bullet \boldsymbol{u}_x) + F_{T_2}(\boldsymbol{T}_2 \bullet \boldsymbol{u}_x) \\ F_n(\boldsymbol{N} \bullet \boldsymbol{u}_y) + F_{T_1}(\boldsymbol{T}_1 \bullet \boldsymbol{u}_y) + F_{T_2}(\boldsymbol{T}_2 \bullet \boldsymbol{u}_y) \\ F_n(\boldsymbol{N} \bullet \boldsymbol{u}_z) + F_{T_1}(\boldsymbol{T}_1 \bullet \boldsymbol{u}_z) + F_{T_2}(\boldsymbol{T}_2 \bullet \boldsymbol{u}_z) \end{pmatrix}$$
(7)

whereas $\boldsymbol{F}_\epsilon$ was defined directly in terms of the scalar projections on $\boldsymbol{N}$, $\boldsymbol{T}_1$, and $\boldsymbol{T}_2$.

We will now show how these operators P_n and P_T can be used to construct the operators in Eq. (3) from the vector field $\boldsymbol{F}$ in Eq. (6). To this end, we start from the spatial-domain relations between the electric field and electric flux density on the one hand and the definition of the vector field $\boldsymbol{F}$ on the other. We have

$$\boldsymbol{D} = M_\varepsilon \boldsymbol{E}, \tag{8a}$$

$$\boldsymbol{F} = P_T \boldsymbol{E} + \alpha P_n \boldsymbol{D}, \tag{8b}$$

where M_ε is the spatial (pointwise) multiplication operator that multiplies by the, generally anisotropic, permittivity tensor $\overline{\overline{\varepsilon}}$. First, we establish a relation between $\boldsymbol{E}$ and $\boldsymbol{F}$. By employing the projection properties, i.e. $P_n P_n = P_n$, $P_n P_T = P_T P_n = 0$, and $P_n + P_T = I$, to the above equations, we obtain

$$P_T \boldsymbol{F} = P_T \boldsymbol{E}, \tag{9a}$$

$$P_n \boldsymbol{F} = \alpha P_n \boldsymbol{D} = \alpha P_n M_\varepsilon (P_n \boldsymbol{E} + P_T \boldsymbol{E})$$
$$= \alpha P_n M_\varepsilon (P_n \boldsymbol{E} + P_T \boldsymbol{F}). \tag{9b}$$

After rearranging terms, we arrive at

$$\boldsymbol{E} = P_n \boldsymbol{E} + P_T \boldsymbol{E}, \tag{10a}$$

$$P_T \boldsymbol{E} = P_T \boldsymbol{F}, \tag{10b}$$

$$P_n \boldsymbol{E} = (P_n M_\varepsilon P_n)^{-1} \left(\frac{1}{\alpha} P_n - P_n M_\varepsilon P_T \right) \boldsymbol{F}, \tag{10c}$$

where $(P_n M_\varepsilon P_n)^{-1}$ is the inverse of $(P_n M_\varepsilon P_n)$ on the range of P_n, i.e. $(P_n M_\varepsilon P_n)^{-1}(P_n M_\varepsilon P_n) = P_n$. Note that P_n is equal to the identity at its range. For isotropic media, the operator $(P_n M_\varepsilon P_n)^{-1}$ is simply identical to $M_\varepsilon^{-1} P_n = P_n M_\varepsilon^{-1}$, i.e. the inverse of the permittivity function multiplied by P_n. For general anisotropic media, $(P_n M_\varepsilon P_n)^{-1}$ is of the form $f(x,y,z)\boldsymbol{N}$, where f depends both on the local permittivity and the local orientation of the vector field $\boldsymbol{N}$.

By employing the relation $P_T = I - P_n$, we obtain the linear operator C_ϵ in Eq. (3) as

$$C_\epsilon = I + (P_n M_\varepsilon P_n)^{-1} P_n \left(\frac{1}{\alpha} I - M_\varepsilon \right). \tag{11}$$

In a similar way, we can derive a relation between the electric flux density and the vector field $\boldsymbol{F}$. We finally end up with

$$\overline{\overline{\varepsilon}} \bullet C_\epsilon = M_\varepsilon \left[I + (P_n M_\varepsilon P_n)^{-1} P_n \left(\frac{1}{\alpha} I - M_\varepsilon \right) \right] = M_\varepsilon C_\epsilon. \tag{12}$$

In the above operator representation, it is essential that the spectral-domain counterpart of the operator product $M_\varepsilon C_\epsilon$ is constructed as a *single* operator in the form of the Laurent rule to maintain the rationale behind the Fourier factorization rules [11]. This is because M_ε and C_ϵ both exhibit a jump at a material interface, i.e.

$$\mathcal{F}\{M_\varepsilon C_\epsilon\} \neq \mathcal{F}\{M_\varepsilon\} * \mathcal{F}\{C_\epsilon\}, \tag{13}$$
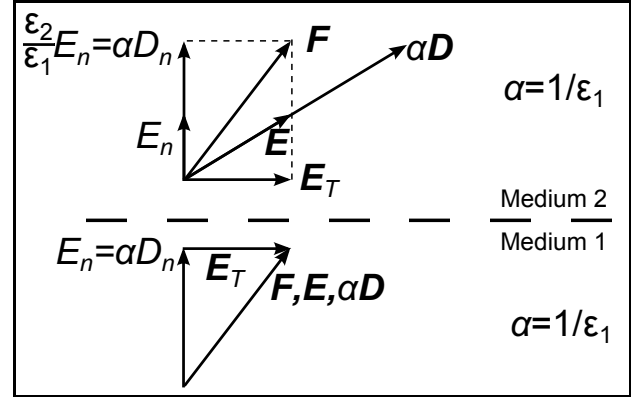
Fig. 1. Scaling of the normal component of the electric flux density $\boldsymbol{D}$ by α to make the normal component D_n locally (in medium 1) equal to the normal component of $\boldsymbol{E}$. Note that the vector field $\boldsymbol{F}$ is continuous across the interface between medium 1 and medium 2.

where $\mathcal{F}\{\cdot\}$ denotes the Fourier transformation and $*$ the discrete convolution.

From the representations of C_ϵ and $\overline{\overline{\varepsilon}} \bullet C_\epsilon$ in Eq. (11) and Eq. (12), we observe that the projection operator P_n only occurs in combination with the operator $\frac{1}{\alpha}I - M_\varepsilon$. Hence, in principle, the support of the latter operator determines the domain over which the normal-vector field $\boldsymbol{N}$ is required to generate the coefficients of the operators C_ϵ and $\overline{\overline{\varepsilon}} \bullet C_\epsilon$. At locations where $\frac{1}{\alpha}I - M_\varepsilon$ is zero, the scaled electric flux density, i.e. $\alpha \boldsymbol{D}$, and the electric field $\boldsymbol{E}$ become locally indistinguishable. This is schematically drawn in Figure 1 for the case of two isotropic media, i.e. $\boldsymbol{D}$ and $\boldsymbol{E}$ are aligned in each medium, and the scaling parameter α is chosen as the inverse permittivity of the bottom medium. The figure shows that all fields $\alpha \boldsymbol{D}$, $\boldsymbol{E}$, $\boldsymbol{F}$ are aligned in medium 1, but the alignment does not hold for the field $\boldsymbol{F}$ in medium 2. However, the field $\boldsymbol{F}$ is continuous in all its components across the material interface. As a consequence of the choice for α, we have for medium 1

$$\boldsymbol{F} = P_T \boldsymbol{E} + \alpha P_n \boldsymbol{D} = P_T \boldsymbol{E} + P_n \left(\frac{\boldsymbol{D}}{\varepsilon_1} \right) = P_T \boldsymbol{E} + P_n \boldsymbol{E} = \boldsymbol{E}, \quad \textbf{(14)}$$

and therefore the electric field is perfectly reproduced by the field $\boldsymbol{F}$. By choosing a basis that is independent of the normal-vector field, such as the Cartesian basis in Eq. (7), the generation of a normal-vector field in medium 1 becomes obsolete. This is in contrast with the framework employed in [1], where the normal-vector field is generated and needed over the entire computational domain.

C. Local normal-vector fields for isotropic media

For the important class of isotropic dielectric media, we can choose the scaling function α such that the operator $\frac{1}{\alpha}I - M_\varepsilon$ in Eq. (11) and Eq. (12) only has local support. We distinguish the following choices for α:

1 A first choice is to set α to a constant equal to the inverse of the (local) host-medium permittivity. This leads to the consequence that the normal-vector field is only required in regions where the permittivity is different from the host-medium permittivity.

2 A second choice is similar to the first one by again choosing α as being constant. However, depending on the grating

structure, it may be more advantageous to choose a different constant by choosing it equal to the inverse permittivity of an object. In general it is beneficial to define the normal-vector field on a geometry that does not involve the boundaries of the unit cell, since for such geometries the normal-vector fields can be rotation and shift invariant.

3 A third choice is to let α be a continuous function, such that it is a *smoothed* version of the original inverse permittivity function, e.g. via tri-linear interpolation or averaging by a Gaussian window. In that case, the normal-vector field is only required in the direct vicinity of the interface between materials and it becomes even more localized. However, the resulting integrals that have to be computed are typically more difficult. By selecting where to start the transition to gradually change from one permittivity to the other, it is possible to end up with localized normal-vector fields that are needed on only one side of the interface between two media.
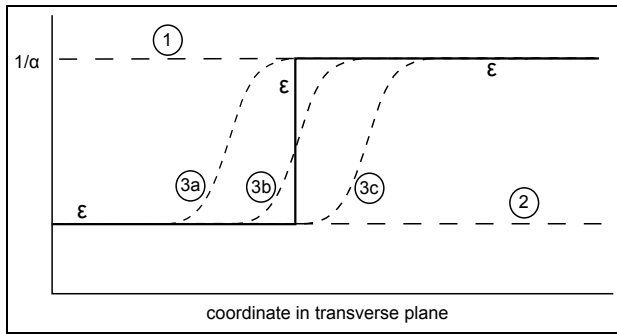
Fig. 2. The choice for the scaling function α against a jump in the permittivity function ε that is indicated by the solid line. The continuous function $1/\alpha$ is plotted by two dashed lines (option 1 and 2) and three dashed curves for three possible choices for the third option, indicated by 3a, 3b, and 3c. The normal-vector field is only required in regions where $1/\alpha$ is different from the permittivity ε.

The three options are further illustrated in Figure 2 and the lines are labeled according to the numbering above. In this figure, the third option is further elaborated with three smooth dashed curves for $1/\alpha$ near a jump in the permittivity function in the transverse plane. For each of the three curves, the normal-vector field is needed only in the area where $1/\alpha$ is different from ε. Hence, for Curve 3a, the normal-vector field is only needed on the left-hand side of the jump, whereas for Curve 3c the normal-vector field is only needed in a small region to the right-hand side of the jump. For Curve 3b, the normal-vector field is needed on both sides of the jump, but still in a limited region, which can be advantageous when a second jump in the permittivity follows close to the first jump.

We note that the above choices also work out for somewhat more general setups with partial anisotropy, as long as the subdomain on which we do not need to generate the normal-vector field is isotropic, such as in case of an anisotropic grating in an isotropic host medium where we choose to generate the normal-vector field inside the grating.

To further illustrate that the proposed framework also includes cases where a host medium is not readily identified, we consider the case of the double sinusoidal grating and the proposed normal-vector field in [1], Section 3.D. Here, the boundary between two dielectric homogeneous halfspaces is given by a product of two sine functions, one for each direction of periodicity in the transverse plane. Translated to the situation discussed here, where the transverse plane is the xy plane, the corresponding description of the boundary between the medium above, with permittivity ε_a, and the medium below, with permittivity ε_b is given by

$$z = g(x,y) = (H/2) \sin\left(\frac{2\pi x}{d_x}\right) \sin\left(\frac{2\pi y}{d_y}\right). \qquad \textbf{(15)}$$

The normal-vector field was chosen to be independent of the longitudinal direction, which is the z direction here. The resulting expression for the normal-vector field N, expressed in the Cartesian components, is

$$N = \frac{1}{\sqrt{(\partial_x g(x,y))^2 + (\partial_y g(x,y))^2 + 1}} \begin{pmatrix} \partial_x g(x,y) \\ \partial_y g(x,y) \\ -1 \end{pmatrix}. \qquad \textbf{(16)}$$

The construction that we propose is independent of the specific choice for the normal-vector field. The only concern is to generate a function $\alpha(x,y,z)$, such that $1/\alpha$ is identical to the permittivity of the medium in a region of choice. If we choose $\alpha = 1/\varepsilon_a$, then we need to employ the normal vector field on the domain below the separation boundary of Eq. (15), over the entire height of the grating, but not on the domain above the separation boundary. If we choose $\alpha = 1/\varepsilon_b$, then the normal-vector field is only required on the domain above the separation boundary over the entire height of the profile. To further confine the region on which the normal-vector field is needed, we can construct the function $1/\alpha(x,y,z)$ equal to a smooth version of the permittivity profile. There are many ways to achieve this. One particular example is to use a description of the grating permittivity profile as

$$\varepsilon(x,y,z) = \varepsilon_a + (\varepsilon_b - \varepsilon_a)H(g(x,y) - z), \qquad \textbf{(17)}$$

where $H(\cdot)$ is the Heaviside unit-step function. By replacing $H(g(x,y) - z)$ by a function $U(g(x,y) - z)$ that smoothly evolves from zero to one, similar to the curves 3a, b and c in Figure 2, we obtain a realization of a smooth permittivity profile, i.e.

$$\varepsilon_{smooth}(x,y,z) = \varepsilon_a + (\varepsilon_b - \varepsilon_a)U(g(x,y) - z), \qquad \textbf{(18)}$$

and we choose $\alpha(x,y,z) = 1/\varepsilon_{smooth}(x,y,z)$. In the regions where $\varepsilon(x,y,z) = \varepsilon_{smooth}(x,y,z)$, Eq. (11) and Eq. (12) demonstrate that the normal-vector field does not play a role and its definition and generation is not needed there. In this way, we can restrict the explicit definition of the normal-vector field to a limited region that includes the separation boundary between the two media.

D. Expressions for C_ϵ and $\overline{\overline{\epsilon}} \bullet C_\epsilon$ for isotropic media

For isotropic media, we ease the notation by denoting the permittivity multiplication operator M_ε by the scalar function $\varepsilon(x,y,z)$ and the Cartesian components of the normal-vector field N by n_x, n_y, and n_z. Through the definition of the projection operator P_n the operator C_ϵ can be decomposed in Carte-

sian components $C_{i,j}$ where $i,j \in \{x,y,z\}$ as

$$C_\epsilon \boldsymbol{F} = \begin{pmatrix} C_{xx} & C_{xy} & C_{xz} \\ C_{yx} & C_{yy} & C_{yz} \\ C_{zx} & C_{zy} & C_{zz} \end{pmatrix} \begin{pmatrix} F_x \\ F_y \\ F_z \end{pmatrix}. \tag{19}$$

To write down expressions for these matrix elements, we note that for isotropic media the operator combination $(P_n M_\varepsilon P_n)^{-1} = P_n(\varepsilon)^{-1}$, which significantly simplifies the expression $(P_n M_\varepsilon P_n)^{-1} P_n((\alpha)^{-1}I - M_\varepsilon) = P_n[(\alpha\varepsilon)^{-1} - 1]$. Hence, in the spatial domain the components $C_{i,j}$ are given by

$$C_{i,j}(x,y,z) = \delta_{i,j} + n_i(x,y,z)n_j(x,y,z)\left[\frac{1}{\alpha(x,y,z)\varepsilon(x,y,z)} - 1\right], \tag{20}$$

where $\delta_{i,j}$ is the Kronecker delta. Similarly, the Cartesian components $\overline{\overline{\epsilon}}C_{i,j}$ of $\overline{\overline{\epsilon}} \bullet C_\epsilon$ are given by

$$\begin{aligned} \overline{\overline{\epsilon}}C_{i,j}(x,y,z) &= \varepsilon(x,y,z)\delta_{i,j} \\ &+ n_i(x,y,z)n_j(x,y,z)\left[\frac{1}{\alpha(x,y,z)} - \varepsilon(x,y,z)\right]. \end{aligned} \tag{21}$$

The corresponding spectral-domain elements of $C_{i,j}$ are given by the Fourier transformation

$$\begin{aligned} c_{ij}(m_1,m_2,z) &= \\ &\frac{1}{\|A_u\|} \iint_{A_u} C_{ij}(x,y,z) \exp\left[j\left(k_x^{m_1,m_2}x + k_y^{m_1,m_2}y\right)\right] dxdy, \end{aligned} \tag{22}$$

where A_u denotes the unit cell in the xy plane and $\|A_u\|$ denotes its area. A similar expression holds for the elements of $\overline{\overline{\epsilon}} \bullet C_\epsilon$. This means that we have to compute the Fourier integrals in the transverse xy plane of the coefficients C_{ij} and $\overline{\overline{\epsilon}}C_{i,j}$ for $i,j \in \{x,y,z\}$. We immediately observe that the area of integration can be further reduced to the support of the function $[\varepsilon(x,y,z)\alpha(x,y,z) - 1]$, as was discussed in the preceding section. A second observation is that the expressions for P_n in Eq. (4) and $P_T = I - P_n$ are insensitive for the choice for the normal to be pointing inwards or outwards, which is due to the choice for projection operators instead of the use of three vector-to-scalar mappings as proposed in [1].

E. Translation and rotation of the scattering object

We will now concentrate on the case of disjoint isotropic and piecewise homogeneous scattering objects embedded in an isotropic homogeneous host medium with permittivity ε_h. This allows us to further simplify the expressions and even derive analytical expressions for several geometries, see Appendices A and B. For the scaling function α we choose $\alpha = 1/\varepsilon_h$. Consequently, the above Fourier integrals reduce to a sum of integrals over the support of each individual object. More importantly, the normal-vector field depends entirely on the shape of each individual object and not on its orientation in the unit cell or on the presence of other objects. This makes the generation of normal-vector fields completely modular and the normal-vector field has to be defined or generated only on the support of the object. Hence, several disjoint objects within the unit cell can be treated independently and the combination of objects simply results in the sum of the corresponding Fourier integrals. A further consequence is that a translation or rotation parallel to the transverse plane of an individual object can be readily dealt with.

First we reconsider the integrals defined in Eq. (22). It is readily observed that the integrals are composed of the more elementary Fourier integrals Γ_{ij} defined only by the shape and its interior normal-vector field as

$$\begin{aligned} \Gamma_{ij}(\boldsymbol{m},z) &= \\ &\frac{1}{\|A_u\|} \iint_{\text{support}} n_i(x,y,z)n_j(x,y,z) \exp\left[j\left(k_x^{\boldsymbol{m}}x + k_y^{\boldsymbol{m}}y\right)\right] dx\, dy, \end{aligned} \tag{23}$$

where the integral is understood to be defined on the support of the shape under consideration, for a given value of z. As an example, closed-form expressions for Γ_{ij} of a binary grating with elliptic footprint in the xy plane are given in Appendix A. Appendix B provides a general "cut-and-connect" strategy to obtain closed-form expressions for gratings for which the contour of the cross section at a given longitudinal position z can be decomposed into straight lines and circular arcs.

For an arbitrary translation along the $\boldsymbol{c_0}$ in the transverse plane, the transformation gives rise to a a new set of local coordinates. Its consequence is that the coefficients $\Gamma_{ij}(\boldsymbol{m},z)$ are multiplied by the phase $\exp[j(k_x^{\boldsymbol{m}}c_{0x} + k_y^{\boldsymbol{m}}c_{0y})]$.

For a rotation, the situation is somewhat more involved. Due to the mixing of x and y directions, the Cartesian components of the normal-vector field also change with respect to the global Cartesian system as well as the direction of the transverse wave vector $\boldsymbol{k}_T^{\boldsymbol{m}} = (k_x^{\boldsymbol{m}}, k_y^{\boldsymbol{m}})$, which appears in the exponential of the Fourier transformation as an inner product with $\boldsymbol{r}_T = (x,y)$. Since the basis for $\boldsymbol{r}_T$ is transformed by a basis-transformation matrix B, i.e. $\boldsymbol{r}_T' = B\boldsymbol{r}_T$, the vector $\boldsymbol{k}_T^{\boldsymbol{m}}$ needs to be transformed by the inverse-transposed of the same basis transformation, i.e. $\boldsymbol{k}_T^{\boldsymbol{m}\prime} = B^{-T}\boldsymbol{k}_T^{\boldsymbol{m}}$, to maintain the invariance of the inner product. The resulting vector $\boldsymbol{k}_T^{\boldsymbol{m}\prime}$ can be interpreted as a sampling of the vector $\boldsymbol{k}_T$ along the Bravais lattice of the *transformed* reciprocal vectors and the former causes the new coefficients Γ_{ij}' to be written as a fixed linear combination of the coefficients Γ_{ij}, albeit sampled at the new values of $(k_x^{\boldsymbol{m}}, k_y^{\boldsymbol{m}})$ after rotation.

3. LOCAL NORMAL-VECTOR FIELDS FOR GENERAL ANISOTROPIC MEDIA

The localization of the normal-vector field as demonstrated above applies mainly to isotropic media. The restriction is caused by the off-diagonal elements of the permittivity tensor for general anisotropic media, the contribution of which can, in general, not be canceled by a single scalar function, i.e. the operator $\left(\frac{1}{\alpha}I - M_\varepsilon\right)$ is in general not equal zero. This obstacle can be overcome by further modifying the definition of the vector field $\boldsymbol{F}$. This renewed definition of $\boldsymbol{F}$ is given by

$$\boldsymbol{F} = P_T \boldsymbol{E} + \alpha P_n(\boldsymbol{D} - SP_T\boldsymbol{E}), \tag{24}$$

where α is again a non-zero scaling function and S is a scaling operator, which are both *continuous* in the vicinity of material discontinuities. Since both $P_n\boldsymbol{D}$ and $P_T\boldsymbol{E}$ are continuous vector fields, the vector field $\boldsymbol{F}$ is again continuous under the requirements for α and S.

With the previously outlined algebra for the projection operators, see Eq. (9), we obtain the expression

$$\boldsymbol{E} = \left\{I + (P_n M_\varepsilon P_n)^{-1}\left[P_n(\frac{1}{\alpha}I - S)P_n - P_n(M_\varepsilon - S)\right]\right\}\boldsymbol{F}. \tag{25}$$

The operator between square brackets can be made zero locally. The first term between the square brackets disappears by choosing $\alpha = (P_n S P_n)^{-1}$ (to be understood on the range of P_n). Subsequently, by choosing S equal to the (anisotropic) permittivity in a certain region that does not involve discontinuities, for example a constant permittivity tensor M_{ε_h} of the host medium, also the second term between the square bracket is equal to zero in regions where $M_\varepsilon = M_{\varepsilon_h}$. In such a region, the normal-vector field is not required, provided that the basis of the vector field $\boldsymbol{F}$ is again independent of the normal-vector field. The resulting expression for Eq. (25) becomes

$$\boldsymbol{E} = \left\{ I - (P_n M_\varepsilon P_n)^{-1} \left[P_n (M_\varepsilon - M_{\varepsilon_h}) \right] \right\} \boldsymbol{F}. \qquad \textbf{(26)}$$

We note that the expressions for C_ϵ and $\overline{\overline{\epsilon}} \bullet C_\epsilon$ are often more complicated than for the isotropic case, mainly because of the operator $(P_n M_\varepsilon P_n)^{-1}$. In the spatial domain we have

$$(P_n M_\varepsilon P_n)^{-1} = \frac{\boldsymbol{N}}{\boldsymbol{N} \bullet (\varepsilon \boldsymbol{N})} \boldsymbol{N} \bullet, \qquad \textbf{(27)}$$

in which the denominator intertwines both the geometry of the material interfaces and the directions of anisotropy. Consequently, analytical expressions for their Fourier transforms are harder to obtain. In such cases, one could instead resort to quadrature methods for more complicated domains, see e.g. [12–14], to compute the pertaining Fourier integrals.

We note that the definitions for the vector field $\boldsymbol{F}$ in Eq. (6) and Eq. (24) are consistent for the isotropic case, since S will then be a multiple of the identity operator and hence S will commute with P_T and P_n. Consequently, $P_n S P_T$ is identically zero and the choice for α reduces to the previously identified cases of Section C.

4. NUMERICAL RESULTS

We employ the volume-integral equation formulation presented in [4] to generate the numerical results presented here. First, we consider an array of aerial cavities with height $h = 50$ nm and with an elliptical footprint inside a square unit cell, identical to the setup discussed in [3], see Figure 3. The lengths of the major and minor axes of the ellipses are indicated by $2a = 1000$ nm and $2b = 500$ nm, respectively, and the major axis has an angle of 45 degrees with respect to the lattice vectors $\boldsymbol{a}_1 = p\boldsymbol{u}_x$ and $\boldsymbol{a}_2 = p\boldsymbol{u}_y$ that span the unit cell, with $p = 1000$ nm. The ellipses, with relative permittivity $\varepsilon_r = 1$, are embedded in a metallic layer with a thickness identical to the height of the cavities and $\varepsilon_r = 0.8125 - j5.25$ on a glass substrate with $\varepsilon_r = 2.25$. For the normal-vector field, we choose $1/\alpha$ equal to the permittivity of the glass substrate, which means that we define the normal-vector field only on the inside of the ellipses, as indicated by the little arrows inside the ellipses. A normally incident plane wave with wavelength $\lambda = 500$ nm and polarization $[E_x, E_y] = [1,1]$ and $[E_x, E_y] = [1,-1]$ is used to illuminate the grating. The zeroth order diffraction efficiency in reflection is shown in Figure 3 for the normal-vector field as given in Appendix A by the solid line for the $[1,1]$ polarization and the dashed line for the $[1,-1]$ polarization. We have computed the results for 33 sample points for the integration in the z direction and Fourier modes from $-M, \ldots, M$ in both the x and the y direction, where $M = \{2, 4, 6, \ldots, 50\}$. The results for the normal-vector-field formulation are indicated by "NV". As a reference, the hollow bullets and triangles represent the data provided in [3], for the normal-vector field generated through the electrostatic strategy for the cases that were
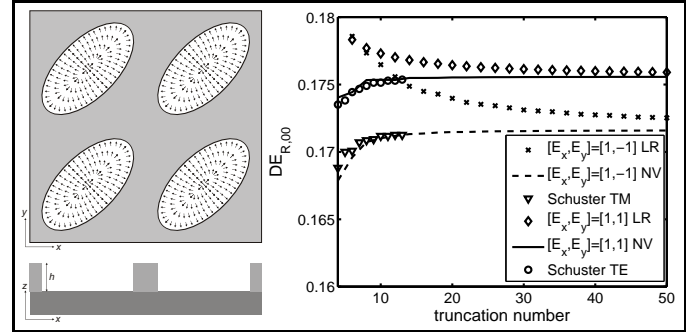
Fig. 3. Left: scattering setup of an array of aerial cavities with elliptic cross section. Right: zeroth-order diffraction efficiency versus the truncation number M of the Fourier expansion. The results for the Laurent rule are indicated by LR and the Normal-vector field results are indicated by NV in the legend. The results indicated by Schuster TE and Schuster TM have been published in [3].
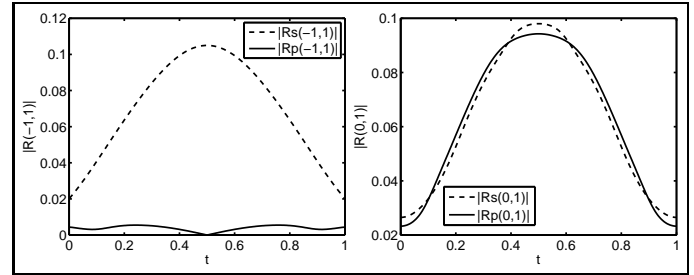
Fig. 4. Reflection coefficients versus parameter t. Left: $|R_s(-1,1)|$ and $|R_p(-1,1)|$ for rotation of the ellipse over an angle $\varphi = \pi t/2$ with respect to the x axis. Right: $|R_s(0,1)|$ and $|R_p(0,1)|$ for the parametrization given in Eq. (29).

referred to as "mainly TE" and "mainly TM" in [3]. The results for the Laurent rule, indicated by "LR", are given for completeness. These results demonstrate once more the much faster convergence when using normal-vector fields in the formulation of field-material interactions in comparison to the direct application of the Laurent rule. The computation for $M = 50$ requires 234 seconds running a single-core process on an Intel i7-2600 CPU @3.40 GHz. Further comparisons between the volume-integral equation, with the normal-vector-field formulation discussed here, and a surface-integral equation can be found in [15–17]. For arrays of circular holes and square holes, the normal-vector field framework defined here was also employed for a volume-integral equation in [4], where it was compared to the combination of RCWA and normal-vector fields in [3].

To further demonstrate the ease of use of geometrical transformations in the local normal-vector field with parameterized normal-vector fields, we consider the same array of elliptical cavities but now starting from the initial situation where the major axis of the ellipse coincides with the x-axis. We parameterize the ellipse in two ways. The first is to rotate the ellipse around its center over an angle

$$\varphi = \frac{\pi}{2} t, \qquad \textbf{(28)}$$

between the major axis and the x-axis, where $t \in [0,1]$. Note that Figure 3 shows the ellipses for $\varphi = 45°$. The second way

is to gradually change the lengths the semi-major axis a and semi-minor axis b of the ellipse by using the parameterizations

$$a(t) = \frac{R}{\sqrt{e_0}} \exp[\ln(e_0) \cos^2(\pi t)], \qquad \textbf{(29a)}$$

$$b(t) = \frac{R}{\sqrt{e_0}} \exp[\ln(e_0) \sin^2(\pi t)], \qquad \textbf{(29b)}$$

where $e_0 = a(0)/b(0)$ is the initial ellipticity of the ellipse for $t = 0$ and R expresses the effective radius $\sqrt{a(0)b(0)}$ of the ellipse. This parametrization is constructed such that the area of the ellipse is constant, i.e. $\pi a(t)b(t) = \pi R^2$, and hence the scattering volume is the same for all values of t. For $t = 1$ the role of the major and minor axes of the ellipse has been interchanged and for $t = 0.5$ the ellipse has become a circle with radius R. Hence, the latter parametrization reveals whether or not an elliptic cavity can be discriminated from a circular cavity while the former reveals whether or not the orientation of the ellipse can be detected. For both cases, we use the same dimensions and materials as described above for the first example and we use 89 (± 44) Fourier modes both in the x and y direction and 33 samples in the z direction. For both parameterizations, the ellipse has its major axis along the x direction for $t = 0$ and along the y direction for $t = 1$. The incident plane wave is normally incident and is polarized as $[E_x, E_y] = [1, 1]$. The absolute value of reflection coefficients in s and p polarization for the Fourier mode (m_1, m_2), i.e. $|R_s(m_1, m_2)|$ and $|R_p(m_1, m_2)|$ respectively, for these two parameterizations are presented in Figure 4. We note that further study has shown that zeroth-order reflection coefficients only vary in the third significant digit as a function of t (not shown here) and are therefore virtually independent of this parameter. Consequently, the orientation and shape of the elliptical cross-section of grating is best monitored via the higher-order modes.

We continue by briefly illustrating the impact of the choice for α on the convergence of the error in the diffraction efficiency and the behavior of the iterative solver. For this, we modify the setup in Figure 3 to the case of aerial cavities with square cross section with an edge length of 500 nm and aligned with the unit-cell boundaries, while keeping the rest of the setup the same. The normal-vector field is chosen to be constant either pointing in the x- or y-direction, where the interface of these two choices lies along the diagonals of the square cavity, extended across the unit cell as indicated in the inset in Figure 5. We now consider three choices for α, all of which are constant throughout the unit cell. The first choice is to choose $1/\alpha$ equal to the permittivity of the aerial cavities, implying that the normal-vector field in only generated and used on the exterior of the cavities. In the second case we choose $1/\alpha$ equal to the permittivity of the metal layer, which corresponds to the normal-vector field to be generated only on the aerial cavities. For the third case we choose $1/\alpha$ as the average of the permittivities of air and metal, which employs a normal-vector field across the entire unit cell. In Figure 5 we illustrate the convergence in terms of the zeroth-order diffraction efficiency compared to a reference value of $DE_{R,ref} = 0.2255$, to which all three cases converge in four significant digits for ± 50 Fourier modes per direction. As can be seen, the convergence rate and absolute accuracy are comparable for the three cases. We also consider the impact on computation time. Since the required Fourier integrals for these cases are analytically available with the help of Appendix B, the computation time is completely dominated by the number of iterations of the iterative solver BiCGstab(2). As can be seen from
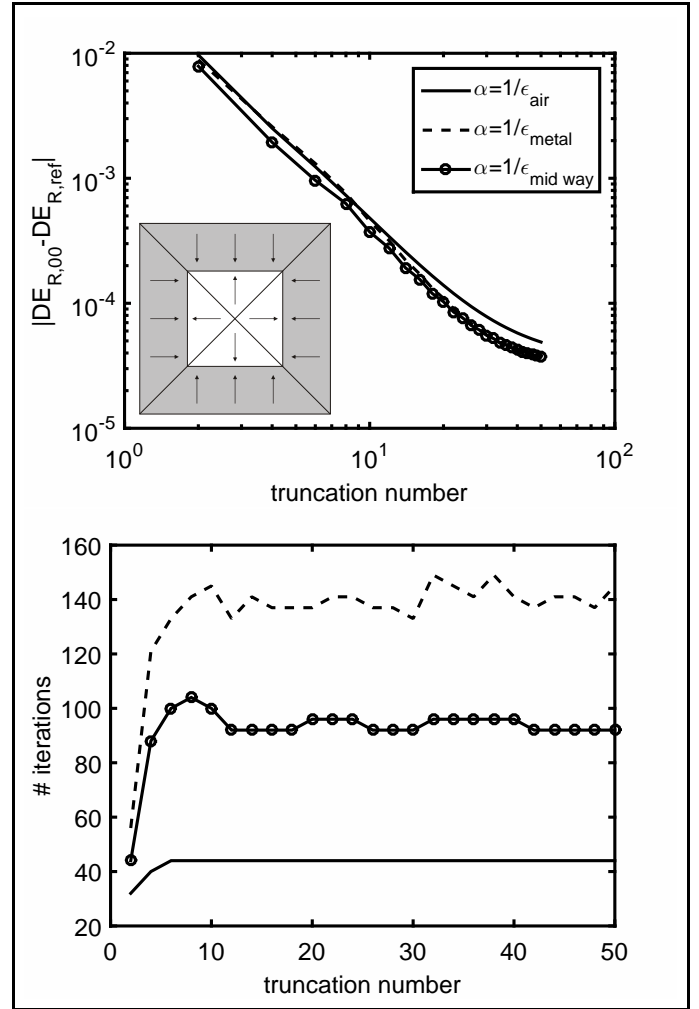

Fig. 5. Influence on the convergence for three choices of α for an array of cavities with square cross section. Solid line: $\alpha = 1/\varepsilon_{air}$, dashed line: $\alpha = 1/\varepsilon_{metal}$, line with circles: $\alpha = 2/(\varepsilon_{air} + \varepsilon_{metal})$. Top: absolute error in the zeroth-order diffraction efficiency with respect to the reference $DE_{R,ref}$. Bottom: number of iterations for BiCGstab(2) to reach 10^{-7}.

Figure 5, the three choices exhibit a significant difference in the number of iterations. Although this example shows that the computation time can be influenced by the choice of alpha, we should stress once more that the choice of alpha for arbitrary complex shapes is predominantly driven by the ease of generating the NV-field. In this particular example this was relatively simple, but for the case of the elliptic aerial cavity, it is more difficult to describe the NV field in parameterized building blocks that vary continuously with the shape parameters.

Subsequently, we give an example of the cut-and-connect strategy for a U-shaped grating, as outlined in Appendix B. The geometry of the U-shape and its position on a layered medium is shown in Figure 6. The corresponding parameters are specified in Table 1, where λ is the wavelength of the incident plane wave in free space. The U-shape is constructed with four circular segments and six polygons. The solid lines indicate interfaces between two dielectric media and the dashed lines on the interior indicate the cuts made between the mesh elements, for which no change in dielectric material is present. The normal-
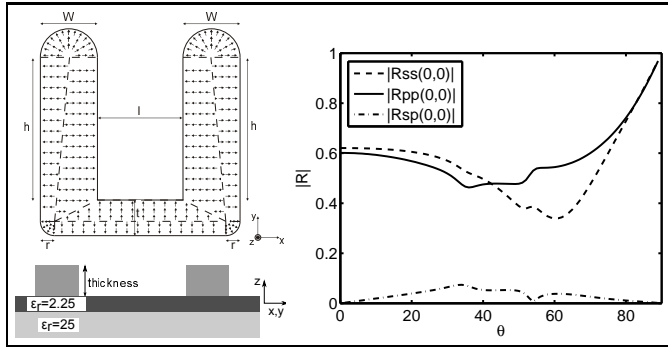
Fig. 6. Top left: contour cross-section of the U-shape decomposed into polygons and circular segments, with parameter values specified in Table 1. The arrows indicate the region on which the normal-vector field is used. Bottom left: cross-section in the xz plane of the layered structure with the U-shape on top. Right: reflection coefficients as a function of the angle θ with respect to the z-axis, in s- and p-polarization for s- and p-polarized incident plane waves.

vector fields are only defined on the inside of the U-shape and are pointing in the radial direction for the circular segments and in the direction normal to the solid line of each polygon. The corresponding choice for $1/\alpha$ equals the permittivity of the upper halfspace, which is free space. The U-shape is positioned in the upper halfspace, on top of a layer with relative permittivity $\varepsilon_r = 2.25$ and thickness 0.25λ. The lower halfspace has a relative permittivity $\varepsilon_r = 25$. The unit cell has lattice vectors $a_1 = \frac{\lambda}{2}u_x$ and $a_2 = \frac{\lambda}{2}u_y$. Owing to the definition of local normal-vector fields per elementary shape, computing the Fourier coefficients for the corresponding shapes is simple and numerically efficient since analytic expressions are directly available. For the simulation, we employ 41 Fourier modes in both the x- and the y-direction and 41 samples in the z-direction. Figure 6 shows the modulus of the zeroth-order reflection coefficients $\left|R_{ij}(0,0)\right|$, where i denotes the polarization of the reflected wave and j the polarization of the incident wave. The results are given for a scan along the angle $\theta = \{0, 1, \ldots, 89\}$ with respect to the z-axis for fixed angle $\phi = 0°$, i.e. along the x-axis. We note that in this case $\left|R_{sp}(0,0)\right| = \left|R_{ps}(0,0)\right|$, owing to the mirror symmetry in the U-shape.

Table 1. Parameters of the U-shape.

parameter	value
h	0.20λ
l	0.25λ
r	0.015λ
t	0.075λ
w	0.06λ
ε_r	6.25
thickness	0.4λ

Finally, we consider a grating with a three-dimensional profile, for which the normal-vector field has components in all

three Cartesian directions. The grating consist of a unit cell with four equally sized frustums in a checker-board pattern, where two frustums are pointing upwards and two are pointing downwards. Together, the surfaces of the frustums, excluding their ground planes, form the boundary between the upper halfspace and the lower halfspace. The setup is shown in Figure 7 and it somewhat resembles a double-sinusoidal grating. The interiors of upward-pointing frustums have a permittivity identical to the permittivity of the bottom halfspace, while the interiors of the downward-pointing frustums have a permittivity equal to the permittivity of the upper halfspace. Each frustum has a square ground plane with edge length w_b at $z = 0$ and a smaller square plane with edge length $w_t = w_b/2$ parallel to and symmetrically positioned above the ground plane at $z = \pm h$. The height of the frustums is $h = w_b/2$. The normal-vector field is only generated on the interior of the frustums, up to and including the boundary of the frustum. To this end, each frustum is divided into four smaller elements by making cuts along the diagonal planes of the corresponding pyramids. Each of these elements then has a normal-vector field that is constant across its entire volume. For this situation, the integrals defined in Eq. (22) for C_ϵ and $\overline{\overline{\epsilon}} \bullet C_\epsilon$ are computed by means of Appendix B. The choices for $1/\alpha$ are then equal to the permittivity of the upper halfspace for $z > 0$ and the permittivity of the lower halfspace for $z < 0$. We note that the top and bottom squares with edge length w_t do not require a normal-vector field orthogonal to their planes, owing to the fact that the computational domain is truncated at these planes. Consequently, the discontinuity in the fields across these planes is automatically accounted for in the discretization of the volume integral equation.

The upper halfspace is free space, while the lower halfspace has a relative permittivity $\varepsilon_r = 2.47$. The grating is illuminated by a plane wave with wavelength $\lambda = 2w_b$, coming from the upper halfspace. The bottom part of Figure 7 shows the zeroth-order reflection coefficients as a function of the angle θ with respect to the z-axis. The reflection coefficients are shown in s- and p-polarization for incidents fields in s- and p-polarization, respectively, in the plane $\phi = 30°$, the angle with the x-axis. For the simulation, 41 Fourier modes per periodic direction have been used, together with 51 sample points for the integration in the z-direction.

5. CONCLUSION

We have presented an adapted version of the normal-vector-field formulation that supports the concept of localized normal vector fields that are tied to a scattering object only, for both isotropic and anisotropic materials. This yields a flexible framework to deal with multiple and composite shapes that can readily be translated and rotated. Numerical results have been provided to illustrate the capability of the local normal-vector-field framework.

REFERENCES

1. E. Popov and M. Nevière, "Maxwell equations in Fourier space: fast-converging formulation for diffraction by arbitrary shaped, periodic, anisotropic media," J. Opt. Soc. Am. A **18**, 2886–2894 (2001).
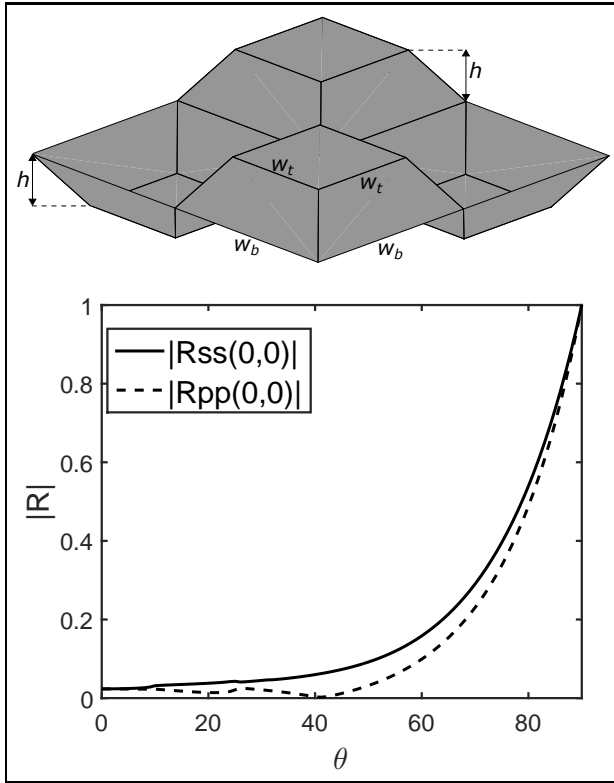
Fig. 7. Top: checkerboard pattern of frustums pointing up and down, as a separation between a free-space upper halfspace and a bottom halfspace with relative permittivity $\varepsilon_r = 2.47$. Bottom: zeroth-order reflection coefficients as a function of the angle θ with respect to the z-axis, in s- and p-polarization for s- and p-polarized incident plane waves, respectively. The plane of incidence is the plane $\phi = 30°$, where ϕ is the angle with respect to the x-axis.

2. E. Popov and M. Nevière, "Grating theory: new equations in Fourier space leading to fast converging results for TM polarization," J. Opt. Soc. Am. A **17**, 1773–1784 (2000).

3. T. Schuster, J. Ruoff, N. Kerwien, S. Rafler, and W. Osten, "Normal vector method for convergence improvement using the RCWA for crossed gratings," J. Opt. Soc. Am. A **24**, 2880–2890 (2007).

4. M. C. van Beurden, "A spectral volume integral equation method for arbitrary bi-periodic gratings with explicit Fourier factorization," Progress In Electromagnetics Research B **36**, 133–149 (2012).

5. T. Magath, "Coupled integral equations for diffraction by profiled, anisotropic, periodic structures," IEEE Trans. Ant. Propagat. **54**, 681–686 (2006).

6. A. A. Shcherbakov and A. V. Tishchenko, "New fast and memory-sparing method for rigorous electromagnetic analysis of 2D periodic dielectric structures," Journal of Quantitative Spectroscopy and Radiative Transfer **113**, 158–171 (2012).

7. S. Rafler, P. Götz, M. Petschow, T. Schuster, K. Frenner, and W. Osten, "Investigation of methods to set up the normal vector field for the differential method," in "Proc. SPIE," (2008), p. 69950Y.

8. P. Götz, T. Schuster, K. Frenner, S. Rafler, and W. Osten, "Normal vector method for the RCWA with automated vector field generation," OPTICS EXPRESS **16**, 17295–17301 (2008).

9. P. Lalanne and G. M. Morris, "Highly improved convergence of the coupled-wave method for TM polarization," J. Opt. Soc. Am. A **13**, 779–784 (1996).

10. G. Granet and B. Guizal, "Efficient implementation of the coupled-wave method for metallic lamellar gratings in TM polarization," J. Opt. Soc. Am. A **13**, 1019–1023 (1996).

11. L. Li, "Use of Fourier series in the analysis of discontinuous periodic structures," J. Opt. Soc. Am. A **13**, 1870–1876 (1996).

12. A. Sommariva and M. Vianello, "Product Gauss cubature over polygons based on Green's integration formula," BIT Numerical Mathematics **47**, 147–177 (2007).

13. A. Sommariva and M. Vianello, "Gauss-Green cubature and moment computation over arbitrary geometries," Journal of Computational and Applied Mathematics **231**, 886–896 (2009).

14. G. Gabard, "Exact integration of polynomial-exponential products with application to wave-based numerical methods," Commun. Numer. Meth. Engng **25**, 237–246 (2008).

15. P. Jorna, V. Lancellotti, and M. C. van Beurden, "SIE approach to scattered field computation for 2D periodic diffraction gratings in 3D space consisting of high permittivity dielectric materials and plasmonic scatterers," in "International Conference on Electromagnetics in Advanced Applications," (2014).

16. P. Jorna, V. Lancellotti, and M. C. van Beurden, "Formulation and implementation of boundary integral equations for scattering by doubly periodic plasmonic and dielectric structures of infinite lateral extent," in "International Conference on Electromagnetics in Advanced Applications," (2015).

17. P. Jorna, V. Lancellotti, and M. C. van Beurden, "Computational aspects of 2D-quasi-periodic-Green-function computations for scattering by dielectric objects via surface integral equations," Progress In Electromagnetics Research B **63**, 49–66 (2015).

18. E. Popov, ed., *Gratings: Theory and Numeric Applications* (Institut Fresnel, Université d'Aix-Marseille, 2014), second revisited ed.

19. I. Gradshteyn and I. Ryzhik, *Table of Integrals, Series and Products* (Academic Press, 1980).

APPENDIX: EXPRESSIONS FOR SHAPE FUNCTIONS

A. The ellipse

For a binary grating with an elliptic footprint with major axis along the x direction and minor axis along the y-direction, we employ the following parametrization to describe the position of the boundary in the Cartesian (x, y) coordinates

$$\boldsymbol{r} = \begin{pmatrix} a\cos\phi \\ b\sin\phi \end{pmatrix} = a \begin{pmatrix} \cos\phi \\ e\sin\phi \end{pmatrix}, \tag{30}$$

where a is the radius along the major axis and b is the radius along the minor axis, ϕ the azimuthal angle and $e = \frac{b}{a}$ the ellipticity. This has the advantage that an analytical expression for Γ_{ij} can be derived. The normal-vector field can be derived as

$$\boldsymbol{n} = \frac{1}{\sqrt{e^2\cos^2\phi + \sin^2\phi}} \begin{pmatrix} e\cos\phi \\ \sin\phi \end{pmatrix}. \tag{31}$$

We note that the above normal-vector field is equivalent to the Cartesian expressions provided in Section 7.7 in [18].

Through the identities in [19], Formulas 8.511.4(c), 3.613.1, and 8.471, we can express the final integrals in terms of the Bessel functions of the first kind J_n as

$$\begin{aligned}
\Gamma_{ij}(m_1, m_2) = \frac{1}{\|A_u\|} &\left\{ \frac{ea^2}{R} J_1(R)\, \Phi_{ij}(0) \right. \\
&+ \frac{ea^2}{R^2} 4[1 - J_0(R)] \sum_{k=1}^{N_b} (-1)^k k\, \Phi_{ij}(k) + 2\frac{ea^2}{R} J_1(R) \sum_{k=1}^{N_b} \Phi_{ij}(k) \\
&\left. - 8\frac{ea^2}{R^2} \sum_{m=1}^{N_b - 1} J_{2m}(R) \left[\sum_{k=m+1}^{N_b} [(-1)^k k - (-1)^m m]\, \Phi_{ij}(k) \right] \right\},
\end{aligned} \tag{32}$$

for $i, j \in \{x, y\}$ and N_b is the number of terms that is retained in the summation over the even Bessel functions. Further,

$$R \equiv a\sqrt{(k_x^m)^2 + (ek_y^m)^2}. \tag{33}$$

and

$$\left\{ \begin{array}{c} \Phi_{xx}(k) \\ \Phi_{xy}(k) \\ \Phi_{yy}(k) \end{array} \right\} = \left\{ \begin{array}{c} \frac{2\pi e}{(1+e)^2}\cos(2kc)\left(\frac{1-e}{1+e}\right)^{k-1} \\ \frac{2\pi e}{(1+e)^2}\sin(2kc)\left(\frac{1-e}{1+e}\right)^{k-1} \\ -\frac{2\pi e}{(1+e)^2}\cos(2kc)\left(\frac{1-e}{1+e}\right)^{k-1} \end{array} \right\} \tag{34}$$

$$= \left\{ \begin{array}{c} \frac{2\pi e}{1+e} \\ 0 \\ \frac{2\pi}{1+e} \end{array} \right\} \quad \text{(for } k = 0), \tag{35}$$

where

$$c = \arctan\left(\frac{ek_y^m}{k_x^m}\right) \tag{36}$$

Note that for the case of a circle ($e = 1$) only the terms for $k = 0, 1$ are non-zero. The required number of terms N_b in the series can be determined by exploiting the exponential decay of the Bessel functions $J_n(x)$ for increasing order n and fixed argument x. This behavior occurs once the order n is larger than the argument x of the Bessel functions.

B. Cut-and-connect strategy

A particularly powerful method for generating the normal-vector fields and closed-form expressions for Γ_{ij} for more arbitrary shapes is obtained when shapes can be decomposed in elementary shapes for which the Γ_{ij} integral has a closed form suited for fast computation. By summing up the relevant Γ_{ij} integrals for each elementary shape at a particular Fourier mode index, the representation of the overall Γ_{ij} can be easily obtained. Of course, the class of elementary shapes must be large enough to generate all relevant more complex shapes. Here we consider elementary shapes of polygonal type with the following properties.

- Each polygon has at most one edge that corresponds to a material interface. Alternatively, all edges of the polygon that coincide with a material interface are parallel.

- The normal-vector field across the entire polygon is constant and must be perpendicular to the material interface.

- If there is no material interface, the normal-vector field can be chosen arbitrarily, but constant.

Any arbitrary shape - or approximation thereof - can in principle be approximated through a mesh of these polygonal shapes. The expressions for the Γ_{ij} are particularly simple, owing to the constant nature of the normal-vector field and the observation that Gauss's theorem allows to reduce the integral over the support of the polygon to a sum of line integrals along all the edges of the polygon, through the identity

$$\iint\limits_{D} \exp\left[j(\mathbf{k}_t \cdot \mathbf{r}_t)\right] dxdy = -\oint\limits_{C} j(\mathbf{k}_t \cdot \mathbf{n}_t)\frac{\exp\left[j(\mathbf{k}_t \cdot \mathbf{r}_t)\right]}{(\mathbf{k}_t \cdot \mathbf{k}_t)}d\ell, \tag{37}$$

where the subscript t indicates a vector in the xy plane, $\mathbf{r}_t = (x, y)$, and $\mathbf{k}_t$ is a vector independent of x and y. Further, C is

the bounding contour of D, $\mathbf{n}_t$ is the outward pointing normal on C in the xy plane, and $d\ell$ is the line element along C.

We note that expressions for circular or annular segments, where the material interface is the circular arc, are readily obtained by following the steps from the previous section in this appendix.